Optomechanical discrete-variable quantum teleportation scheme

Samuel Pautrel, Zakari Denis, Jérémy Bon, Adrien Borne, Ivan Favero

Optomechanical discrete-variable quantum teleportation scheme

Samuel Pautrel, Zakari Denis, Jérémy Bon, Adrien Borne, and Ivan Favero*
Matériaux et Phénomènes Quantiques, Université de Paris, CNRS UMR 7162, 10 rue Alice Domon et Léonie Duquet, 75013 Paris, France

(Received 29 April 2020; accepted 26 May 2020; published 16 June 2020)

We propose an experimental protocol to realize discrete-variable quantum teleportation using optomechanical devices. The photonic polarization superposition state of a single photon is teleported to a phononic superposition of two micromechanical oscillators by means of photon-phonon entanglement generation and optical Bell state measurement using two-photon interference. Verification of the protocol is performed by coherent state transfer between the mechanical devices and light. Simulations show the feasibility of the proposed scheme at millikelvin temperatures using state-of-the-art gigahertz optomechanical devices.

DOI: 10.1103/PhysRevA.101.063820

I. INTRODUCTION

Quantum teleportation [1] consists in transferring (teleporting) an arbitrary quantum state between two objects that are possibly distinct in nature, and possibly distant from one another. Quantum teleportation protocols always rely on entanglement, a resource at the heart of several quantum technologies, and they have been implemented in a variety of systems: first with optical photons [2,3], then among distinct atoms of a molecule [4] or of a linear trap [5–7], and more recently from a photon to a solid-state spin [8] and between two solid-state qubits [9,10]. In an effort to extend these teleportation principles to a macroscopic scale, protocols were theoretically proposed to transfer quantum states between light and vibrating mechanical systems, in the case of continuous variables [11–14]. However, to date there is no report of optomechanical quantum teleportation following these propositions, and an experimental gap remains. The emergence of nanoscale gigahertz optomechanical resonators [15–17] may allow us to fill this gap, as suggested by recent experiments in the quantum realm such as the optical entanglement of mechanical systems [18] and the test of related Bell inequalities [19].

In this paper, we introduce a discrete-variable optomechanical quantum teleportation scheme compatible with current technology. In the present scheme, the state of a single-photon polarization-encoded qubit is teleported onto a dual-rail phononic qubit encoded in two mechanical resonators. Our approach relies on measurement-induced entanglement in the experimentally relevant weak-coupling and good-cavity (resolved-sideband) regime, with mechanical systems originally cooled close to their ground state. We analytically and numerically model the full protocol, and quantify its resilience against various sources of noise and disorder. The calculated efficiencies and fidelities, the latter exceeding 0.9 with realistic parameters, indicate that storing the quantum information conveyed by a single photon within a long-lasting mechanical excitation is now an objective at reach.

*ivan.favero@u-paris.fr

II. PRINCIPLE

The scheme we propose uses two identical optomechanical resonators with an optical resonant frequency ω_c coupled to a mechanical mode of angular frequency Ω_m with a single-photon coupling rate g_0, placed at millikelvin temperatures in order to initially reside in their mechanical ground state. The protocol setup is depicted in Fig. 1. Each resonator is placed in one arm of a balanced Mach-Zehnder interferometer. The devices are driven with a linearly polarized (say, horizontally polarized H) laser and the light at the output of the two arms is recombined on a polarizing beam splitter (PBS) after rotation of one arm's polarization with a half-wave plate ($\lambda/2$). The resulting light is bandpass filtered with a high-finesse Fabry-Perot cavity in order to select the photons scattered at the resonant frequency ω_c and then directed to one of the two measurement units involving single-photon detectors (SPDs), which respectively implement Bell state measurement and quantum state tomography. The protocol we present is reminiscent of a former protocol involving ions [7], and starts with both mechanical resonators in their ground state ($n_1 = n_2 = 0$, where n is the phonon number). It consists of two steps: (i) teleportation of the quantum information from a photonic qubit to a phononic qubit, and (ii) optical readout of the teleported state.

In (i) a blue-detuned H-polarized pulse (frequency $\omega_+ = \omega_c + \Omega_m$) generates a phonon in one of the two optomechanical devices OM_1 or OM_2 with low probability via a cavity-enhanced optomechanical (Raman) interaction (Stokes process). The creation of such a delocalized mechanical excitation is concomitant with the presence of one photon at the cavity frequency ω_c at the output of the interferometer, after filtering the much stronger blue-detuned pump tone [18]. In order to erase the which-path information, the optical cavity frequencies must be as close as possible to maximize the indistinguishability of their output photons. At this point and in the ideal case, the two mechanical resonators are entangled with the optical output of the Mach-Zehnder in a state proportional to $|01V\rangle + |10H\rangle$, where $|n_1 n_2 P\rangle$ denotes the product state with n_1 phonons in OM_1, n_2 phonons in OM_2 and a photon with polarization $P = H$ or V.

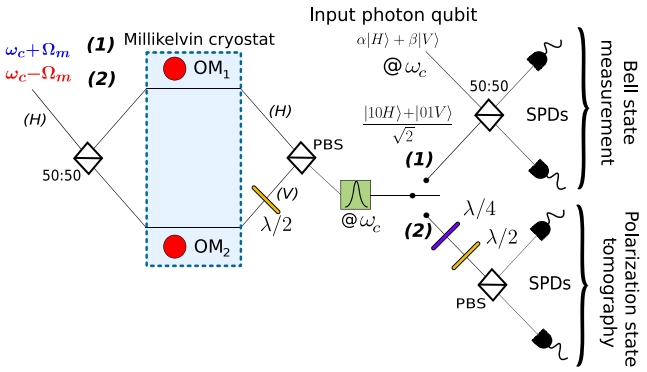

FIG. 1. Schematics of the protocol setup with its two steps. A blue-detuned pulse (1) probabilistically generates a phonon in one of the two resonators, entangling them with the output optical mode. After filtering out the pump tone, we interfere the output photon with an arbitrarily polarized, but otherwise indistinguishable, photon. A coincidence event on the two SPDs heralds the teleportation (see text for details). A red-detuned pulse (2) coherently maps the mechanical state onto a photon whose polarization state is subsequently analyzed by means of quantum optical tomography.

We then perform a two-photon interference experiment on a 50:50 beam splitter between the previous scattered photon and an arbitrarily polarized single photon whose state $|\Phi\rangle = \alpha|H\rangle + \beta|V\rangle$ is to be teleported. Assuming these two photons are spectrally indistinguishable, a coincidence on the two SPDs at the output ports of the beam splitter indicates the projection of the bipartite photonic state in the antisymmetric Bell state $|\Psi^-\rangle = \frac{1}{\sqrt{2}}(|HV\rangle - |VH\rangle)$ before the beam splitter. This is a partial canonical Bell state measurement (BSM). Thus a coincidence event following this blue-detuned pulse heralds the teleportation of arbitrary amplitudes α and β into a bipartite dual-rail phononic state encoded on the two mechanical resonators 1 and 2, $|\Psi^{\rm rot}_{\rm mech}\rangle = \beta|10\rangle - \alpha|01\rangle$ (i).

To retrieve the stored information, we apply (ii) a red-detuned pulse (frequency $\_ = \ c - \Omega_m$) to implement a beam-splitter interaction through cavity-enhanced optomechanical (Raman) scattering (anti-Stokes) and coherently map the mechanical state onto a single photon at $\ c$, whose polarization state is then analyzed by conventional optical quantum state tomography. If not analyzed, the obtained photon could be guided to a remote similar experiment in order to perform teleportation again, propagating the quantum information. The mechanical resonators would then act as quantum memories [20], an approach that appears relevant now that nanomechanical dissipation mechanisms are well understood [21] and promise $Q\times f$ factors (mechanical quality factor times frequency) approaching 10^{20} [21,22].

III. MODEL

A. General model and evolution operators

We start from the Hamiltonian for a driven-dissipative optomechanical system with initial mechanical occupancy $n_0 \ll 1$, resonant cavity frequency $\ c$, optical linewidth κ dominated by the extrinsic decay rate κ_e, mechanical frequency Ω_m and mechanical damping rate γ_m. The optical cavity is driven with a laser at frequency $\ \pm = \ c \pm \Omega_m$. The total Hamiltonian reads:

$$\hat{H} = \hat{H}_0 + \hat{H}_{\rm int} + \hat{H}_{\rm env} + \hat{H}_{dr\pm} \tag{1a}$$

$$\hat{H}_0 = \hbar \ _c\hat{a}^\dagger\hat{a} + \hbar\Omega_m\hat{b}^\dagger\hat{b} \tag{1b}$$

$$\hat{H}_{\rm int} = -\hbar g_0\hat{a}^\dagger\hat{a}(\hat{b}^\dagger + \hat{b}) \tag{1c}$$

$$\hat{H}_{dr\pm} = \hbar(s^*_\pm e^{i \ \pm t}\hat{a} + s_\pm e^{-i \ \pm t}\hat{a}^\dagger), \tag{1d}$$

where $\hat{H}_{\rm int}$ and $\hat{H}_{\rm env}$ account for the optomechanical interaction and for the environment respectively, and $\hat{H}_{dr\pm}$ is the driving term with $|s_\pm| = \sqrt{\kappa P_\pm/\hbar \ \pm}$ the incoming photon flux for a laser power $P_\pm$. $\hat{H}_0$ is the bare Hamiltonian for the two harmonic oscillators where $\hat{a}$ ($\hat{b}$) is the annihilation operator for the optical (mechanical) mode under consideration. Starting from the Heisenberg picture, we rotate our operators with respect to $\hat{H}_0$, following Ref. [23]. We then assume to be in the good-cavity (resolved-sideband) regime, and consider interaction times τ shorter than $2\pi(n_0\gamma_m)^{-1}$ but longer than $2\pi\kappa^{-1}$:

$$n_0\gamma_m \ll \frac{2\pi}{\tau} \ll \kappa \ll \Omega_m. \tag{2}$$

This allows us to neglect all terms rotating faster than Ω_m in the temporal envelope of the cavity field, to ignore the cavity transient behavior, and to neglect mechanical damping [23,24]. Since in the experiment photons are filtered around $\ c$ at the resonator output; we focus below on the component $\hat{a}$ of the cavity operator evolving close to the cavity frequency [23,24], which is linked to the input and output of the cavity through $\hat{a}_{out} = -\hat{a}_{\rm in} + \sqrt{\kappa}\hat{a}$. Neglecting the transient dynamics, the following relations are then obeyed:

$$\hat{a}_{\pm,\rm out} = \hat{a}_{\rm in} + i\sqrt{2\tilde{g}_\pm}\hat{b}^\dagger_\pm \tag{3}$$

$$\frac{d\hat{b}_\pm}{dt} = \pm\tilde{g}_\pm\hat{b}_\pm + i\sqrt{2\tilde{g}_\pm}\hat{a}^\dagger_{\rm in}, \tag{4}$$

under the condition of weak interaction $g_0 \ll \kappa, \ m$. In the terms on the right, note the implication of $\hat{b}$, $\hat{a}_{\rm in}$ for the drive – and of their adjoints for the drive +. $\tilde{g}_\pm = 2g_0^2 n_{c_\pm}/\kappa$ with $n_{c_\pm} = \frac{\kappa P_\pm}{\hbar \ c(\Omega_m^2+\kappa^2/4)}$ the number of intracavity photons at frequency $\ \pm$.

With these approximate relations, we can now model the effect of blue- and red-detuned pulses with an error that we checked to be negligible for the investigated parameter space, when compared to simulations of the dynamics under the action of the complete Liouvillian. A blue drive pulse of duration T_+ with weak power P_+ implements a squeezing operator that creates photon-phonon pairs in equal proportion, while the subsequent red pulse of duration T_- and weak power P_- implements a beam-splitter-like interaction converting phonons into photons at frequency $\ c$, allowing the state transfer from mechanics to optics. In order to describe these two sequences, we introduce the following temporal modes

already considered in Refs. [13,25]:

$$\hat{A}_{\pm,\mathrm{in}}(t) = \sqrt{\frac{2\tilde{g}_{\pm}}{e^{\mp\tilde{g}_{\pm}t}(e^{\tilde{g}_{\pm}t} - e^{-\tilde{g}_{\pm}t})}} \int_0^t dt\, e^{\mp\tilde{g}_{\pm}t}\, \hat{a}_{\mathrm{in}}(t\,) \quad (5a)$$

$$\hat{A}_{\pm,\mathrm{out}}(t) = \sqrt{\frac{2\tilde{g}_{\pm}}{e^{\pm\tilde{g}_{\pm}t}(e^{\tilde{g}_{\pm}t} - e^{-\tilde{g}_{\pm}t})}} \int_0^t dt\, e^{\pm\tilde{g}_{\pm}t}\, \hat{a}_{\pm,\mathrm{out}}(t\,) \quad (5b)$$

and look for evolution operators $\hat{U}_{\pm}(T_{\pm})$ that satisfy $\hat{A}_{\pm,\mathrm{out}}(T_{\pm}) = \hat{U}_{\pm}^{\dagger}(T_{\pm})\hat{A}_{\pm,\mathrm{in}}(T_{\pm})\hat{U}_{\pm}(T_{\pm})$ and $\hat{b}(T_{\pm}) = \hat{U}_{\pm}^{\dagger}(T_{\pm})\hat{b}(0)\hat{U}_{\pm}(T_{\pm})$. As detailed in Appendix A, we find as a solution for the blue pulse:

$$\hat{U}_{+}(T_{+}) = e^{i\tanh q\hat{A}_{+,\mathrm{in}}^{\dagger}\hat{b}^{\dagger}(0)} \times (\cosh q)^{-1-\hat{A}_{+,\mathrm{in}}^{\dagger}\hat{A}_{+,\mathrm{in}}-\hat{b}^{\dagger}(0)\hat{b}(0)} e^{i\tanh q\hat{A}_{+,\mathrm{in}}\hat{b}(0)} \quad (6)$$

with $\cosh q = \exp(\tilde{g}_{+}T_{+})$. For the red pulse we obtain:

$$\hat{U}_{-}(T_{-}) = e^{i\tan r\hat{A}_{-,in}^{\dagger}\hat{b}(0)}(\cos r)^{-\hat{A}_{-,in}^{\dagger}\hat{A}_{-,in}+\hat{b}^{\dagger}(0)\hat{b}(0)} e^{i\tan r\hat{A}_{-,in}\hat{b}^{\dagger}(0)} \quad (7)$$

with $\cos r = \exp(-\tilde{g}_{-}T_{-})$, an expression that strictly coincides with that found in Ref. [25], despite a different ordering choice for operators (see Appendix A).

B. Application to our protocol

We consider now the experimental setup described in Fig. 1, featuring two identical optomechanical resonators OM_i, $i \in \{1, 2\}$ whose mechanical degree of freedom is initially in a thermal state with equal average occupancy $n_{01} = n_{02} = (e^{\hbar\Omega_m/k_BT} - 1)^{-1} \ll 1$. Possible differences between the two resonators and their consequences on the performances of the present protocol are discussed in Appendix C. Since we start in the vacuum state for both optical modes, the initial total density matrix is

$$\rho_{\mathrm{tot,in}} = |00\rangle\langle 00|_{A_1A_2} \otimes \rho_{b_1}^{th}(n_0) \otimes \rho_{b_2}^{th}(n_0), \quad (8)$$

where we adopt back a Schrödinger picture (but rotated by $\hat{H}_0$) and where $\hat{A}_i = \hat{A}_{i,\mathrm{in}}(T)$ and $\tilde{\hat{b}}_i = \hat{b}_i(0)$. The first step of the protocol consists in driving the devices with a blue pulse that generates a phonon delocalized over the two mechanical resonators [18]. We apply the evolution operator for a blue pulse of duration T_+ of strength $\tilde{g}_+$ (tunable via laser power) and obtain the density matrix at the end of the interaction:

$$\rho_{\mathrm{tot,out}} = \hat{U}_{+}^{\mathrm{tot}}(T_{+})\rho_{\mathrm{tot,in}}\hat{U}_{+}^{\mathrm{tot},\dagger}(T_{+}) \quad (9a)$$

$$\hat{U}_{+}^{\mathrm{tot}} = \hat{U}_{+}^{(A_1b_1)} \otimes \hat{U}_{+}^{(A_2b_2)}. \quad (9b)$$

Note that postselecting on the presence of a photon at the interferometer output and tracing on the optical modes would produce a mechanical density matrix close to $|01\rangle\langle 01|_{b_1b_2} + |10\rangle\langle 10|_{b_1b_2}$, such as investigated elsewhere [18]. Here we instead perform a multiple-photon interference with the optical state to be teleported $|\Phi\rangle = \alpha|H\rangle + \beta|V\rangle$ by applying a perfect 50:50 beam-splitter operator $\hat{U}_{BS}$ and postselecting the events where at least one photon goes out of each port. At this stage, the teleportation (i) is performed. We can compute the fidelity $\mathcal{F}_+$ of the mechanical state with respect to $|\Psi_{\mathrm{mech}}^{\mathrm{rot}}\rangle$ as well as the probability p_+ for such a coincidence event to happen. For the subsequent readout of the teleported state (ii), we apply a red-detuned pulse of duration T_- with interaction strength $\tilde{g}_-$ and trace on the mechanical modes, in cases where one photon a least was detected. Similarly, we compute the fidelity $\mathcal{F}_-$ of the obtained optical density matrix with respect to the ideal rotated state $|\Psi_{\mathrm{opt}}^{\mathrm{rot}}\rangle = \beta|H\rangle - \alpha|V\rangle = -\sigma_x\sigma_z|\Phi\rangle$, as well as the probability p_- that a photon was indeed detected.

IV. NUMERICAL SIMULATIONS

We compute numerically the fidelity and probability of success for the two steps (i) and (ii) of the protocol, as a function of the initial occupancy n_0 and of the interaction strengths $\tilde{g}_+T_+$ and $\tilde{g}_-T_-$ for the blue and red pulses. Unless explicitly specified, we work with real and equal amplitudes $\alpha = \beta = 1/\sqrt{2}$.

A. Dependence on the initial phonon occupancy

The results shown in Figs. 2(a) and 2(b) for $\tilde{g}_+T_+/2\pi = \tilde{g}_-T_-/2\pi = 4.9\times10^{-3}$ feature a clear deterioration of the fidelity as n_0 increases, for both steps (i) and (ii). Indeed, a larger initial thermal population of phonons implies a less pure ground state, an error that propagates to the mechanical state obtained after teleportation. The counterpart of this degraded mechanical state is that the probability to obtain coincidences events after the blue pulse (p_+) and to obtain a photon after the red pulse (p_-) also increase, equally drastically. In other words the probability of the protocol to be completed is increased, but at the expense of its fidelity. The increase of p_+ can be understood by an approximate analytical treatment (see Appendix B), while a larger n_0 also implies that a larger number of phonons are available for annihilation by the red pulse, explaining the increase in the probability p_-.

The fidelity $\mathcal{F}_-$ after step (ii) is larger than the mechanical fidelity $\mathcal{F}_+$ after step (i), a result that may appear counterintuitive at first. Indeed, at the end of step (i), the obtained mechanical density matrix has multiphonon terms because of nonzero initial phonon occupancy. Its mapping to an optical density matrix in step (ii) is not faithful since postselection on single anti-Stokes photons at ω_c is performed at that stage. This reduction of the relevant Hilbert space is accompanied by a reduction of information, letting single and multiphonon terms in the mechanical density matrix lead to indistinguishable optical contributions. This purifies the obtained optical state with respect to the mechanical state it was mapped from. The situation is different for the mechanical Hilbert space, whose dimensions must be large enough to cover all significantly populated Fock states, and where the presence of multiphonon terms decrease the fidelity to the target mechanical state.

B. Dependence on interaction strengths

We now choose an initial phonon occupancy of 10^{-3} in order to operate in a regime of large fidelity, a reachable regime with very high mechanical frequency resonators and millikelvin temperatures, and set $\tilde{g}_-T_-/2\pi = 4.9\times10^{-3}$ while we sweep $\tilde{g}_+T_+$. Conversely, we set $\tilde{g}_+T_+/2\pi = 4.9\times10^{-3}$ and sweep $\tilde{g}_-T_-$. The results are shown on Figs. 2(c)–2(f).

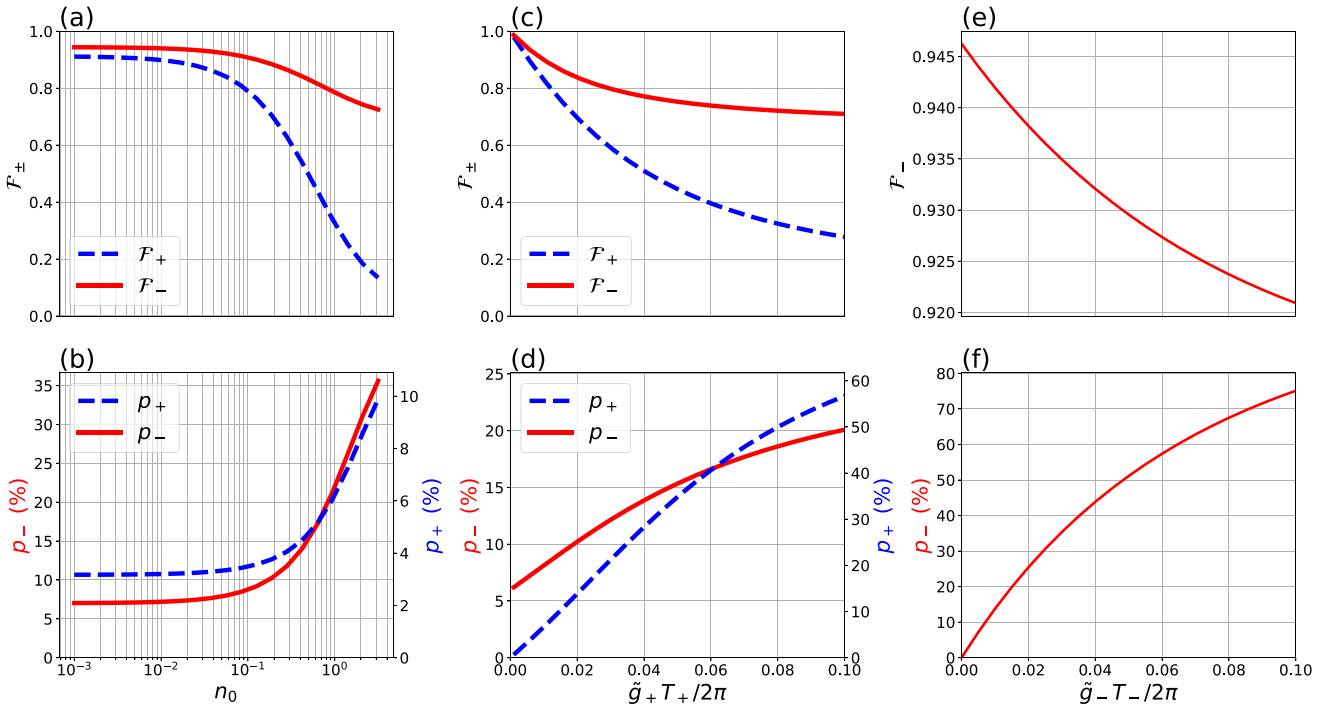

FIG. 2. (a) Fidelities $\mathcal{F}_\pm$ and (b) probabilities of success $p_\pm$ after the two steps of the protocol as a function of the initial phonon occupancy, for a fixed $\tilde{g}_\pm T_\pm/2\pi$ of 4.9×10^{-3}. Blue dashed lines: $\mathcal{F}_+$ of the dual-rail-encoded phononic state with respect to the rotated ideal state $|\Psi^{\rm rot}_{\rm mech}\rangle$, and probability p_+ of successful coincidence event; red solid lines: $\mathcal{F}_-$ of the photon state obtained after state transfer with respect to $|\Psi^{\rm rot}_{\rm opt}\rangle$, and probability p_-. (c) Fidelities $\mathcal{F}_\pm$ and (d) probabilities of success $p_\pm$ as a function of $\tilde{g}_+T_+/2\pi$ while $\tilde{g}_-T_-/2\pi$ is set to 4.9×10^{-3} and n_0 to 10^{-3}. (e) Fidelity $\mathcal{F}_-$ and (f) probability p_- as a function of $\tilde{g}_-T_-/2\pi$ while $\tilde{g}_+T_+/2\pi$ is set to 4.9×10^{-3} and n_0 to 10^{-3}.

As expected, a too strong blue pulse triggers multiple phonon generation that deteriorates the fidelity, while increasing the probability of success of the first step. The results of Figs. 2(e) and 2(f) show that we can increase the red pulse strength in order to increase the probability of success of the second step, while conserving a decent associated fidelity. This is of course in the ideal case in absence of transient heating during the pulse, which would populate higher phonon Fock states [26]. In such case, a strong red-detuned pulse could annihilate more than one phonon, inducing random multiphoton states before the optical tomography. Note that the requirement of small $\tilde{g}_\pm T_\pm$, combined with $T_\pm \gg 2\pi\kappa^{-1}$ translates into the experimentally relevant weak coupling regime $g_0\sqrt{n_{c\pm}} \ll \kappa$.

C. Experimental feasibility

Let us now discuss the feasibility of this scheme with concrete experimental parameters, compatible with recent realizations [18–20,26]:

$\Omega_m/2\pi$ [GHz]	T [mK]	$\kappa_e/2\pi$ [MHz]	$g_0/2\pi$ [kHz]	$T_\pm$ [ns]	$n_{c\pm}$
5.0	20	200	700	10	100

and use the three following dimensionless parameters relevant to the protocol:

n_0	$\tilde{g}_+T_+/2\pi$	$\tilde{g}_-T_-/2\pi$
3×10^{-2}	4.9×10^{-3}	4.9×10^{-3}

which lead to expectations for the fidelities and probabilities of success of the two steps:

$\mathcal{F}_+$	$\mathcal{F}_-$	p_+ [%]	p_- [%]	p_+p_- [%]
0.87	0.93	3.3	7.5	0.25

The condition that the pulse duration is longer than $2\pi\kappa^{-1}$ is respected by a factor of only five in this example, underlining the need for good optical cavities. At equal interaction strength $\tilde{g}T$, the pulse can be made longer at the expense of a lower intracavity photon number, which will degrade the signal to noise ratio (see Appendix C). Still, these results show that our protocol can lead to relatively high fidelities already with realistic parameters.

V. CONCLUSION

We have described an optomechanical discrete variable quantum teleportation scheme that is readily implementable with state-of-the-art optomechanical devices. Based on a

heralded probabilistic principle, this protocol enables teleportation, mechanical storage and further readout of an arbitrary qubit state originally encoded on a single photon. The protocol is expected to allow high fidelity, not only for the storage of the qubit in the mechanical memory ($_+$), but also for the retrieval of the single-photon flying qubit at the output, with an expected fidelity $_-$ reaching 0.93. These features pave the way for future experiments in the realm of quantum communications and memories with optomechanics, a technology that is yet to be explored in this context.

Note added. Recently, a related manuscript was posted [27].

ACKNOWLEDGMENTS

The authors thank Cristiano Ciuti for useful discussions and acknowledge support by the European Research Council through the ERC NOMLI project, and of the Région Ile de France through the SIRTEQ OMQuTe project.

APPENDIX A: EVOLUTION OPERATORS OF OUR MODEL

Starting from the Langevin equations [Eqs. (3) and (4)] and from the definition of the temporal mode [Eqs. (5a) and (5b)], whose exponential shape is an approximation valid in the adiabatic regime $g_0 \ll \kappa$, we obtain below the evolution operators $\hat{U}$. By integrating Eqs. (3) and (4), we reexpress $\hat{A}_{\pm,\mathrm{out}}$ and $\hat{b}_\pm$:

$$\hat{A}_{\pm,\mathrm{out}}(t) = e^{\pm\tilde{g}_\pm t}\hat{A}_{\pm,\mathrm{in}}(t) + i\sqrt{e^{\pm\tilde{g}_\pm t}(e^{\tilde{g}_\pm t} - e^{-\tilde{g}_\pm t})}\hat{b}^\dagger,(0) \tag{A1}$$

$$\hat{b}_\pm(t) = e^{\pm\tilde{g}_\pm t}\hat{b}(0) + i\sqrt{e^{\pm\tilde{g}_\pm t}(e^{\tilde{g}_\pm t} - e^{-\tilde{g}_\pm t})}\hat{A}^{\dagger,}_{\pm,\mathrm{in}}(t). \tag{A2}$$

The procedure to express the evolution operator for the blue pulse (i) obeying $\hat{A}_{+,\mathrm{out}}(t) = \hat{U}_+^\dagger(t)\hat{A}_{+,\mathrm{in}}(t)\hat{U}_+(t)$ and $\hat{b}_+(t) = \hat{U}_+^\dagger(t)\hat{b}(0)\hat{U}_+(t)$ follows closely a work by Truax [28]. By defining $\cosh(q) = e^{\tilde{g}_+ t}$ and $\sinh(q) = \sqrt{e^{2\tilde{g}_+ t} - 1}$, we show that the unitary operator $\hat{U}_+(t) = \exp[iq(\hat{A}_{+,\mathrm{in}}(t)\hat{b}(0) + \mathrm{H.c})]$ realizes the desired rotation. By writing $\hat{U}_+^\dagger(t) = \exp\hat{B}$, we have indeed:

$$\hat{A}_{+,\mathrm{out}}(t) = e^{\hat{B}}\hat{A}_{+,\mathrm{in}}(t)e^{-\hat{B}}$$

$$= \sum_{k\in\mathbb{N}} \frac{1}{k!}\underbrace{[\hat{B},[\hat{B},\ldots,[\hat{B},\hat{A}_{+,\mathrm{in}}(t)]]]}_{k\text{ times}} \tag{A3}$$

$$= \cosh(q)\hat{A}_{+,\mathrm{in}}(t) + i\sinh(q)\hat{b}^\dagger(0), \tag{A4}$$

where we used that the nested commutators equal $q^k\hat{A}_{+,\mathrm{in}}(t)$ for k even and $iq^k\hat{b}^\dagger(0)$ for k odd. Similarly:

$$\hat{b}_+(t) = \cosh(q)\hat{b}(0) + i\sinh(q)\hat{A}^\dagger_{+,\mathrm{in}}(t) \tag{A5}$$

retrieving indeed Eqs. (A1) and (A2).

We express now $\hat{U}_+(t)$ in a more convenient manner. We note that $\hat{U}_+(t) = \exp[iq(\hat{L}_+ + \hat{L}_-)]$ with $\hat{L}_+ = \hat{L}_-^\dagger = \hat{A}^\dagger_{+,\mathrm{in}}(t)\hat{b}^\dagger(0)$, such that by defining $\hat{L}_0 = \hat{L}_0^\dagger = \frac{1}{2}[1 + \hat{A}^\dagger_{+,\mathrm{in}}(t)\hat{A}_{+,\mathrm{in}}(t) + \hat{b}^\dagger_+(0)\hat{b}_+(0)]$, we obtain three generators of the u(1, 1) Lie algebra ($[\hat{L}_-,\hat{L}_+] = 2L_0$, $[\hat{L}_0,\hat{L}_\pm] = \pm L_\pm$). From Eq. (23b) of Ref. [28], one obtains the evolution operator for the blue pulse:

$$\hat{U}_+(t) = e^{i\tanh q\hat{A}^\dagger_{+,\mathrm{in}}\hat{b}^\dagger(0)} \times (\cosh q)^{-1-\hat{A}^\dagger_{+,\mathrm{in}}\hat{A}_{+,\mathrm{in}}-\hat{b}^\dagger(0)\hat{b}(0)}e^{i\tanh q\hat{A}_{+,\mathrm{in}}\hat{b}(0)}. \tag{A6}$$

The procedure to obtain the red pulse (ii) evolution operator is similar and starts by defining $\cos(r) = e^{-\tilde{g}_- t}$ and $\sin(r) = \sqrt{1 - e^{-2\tilde{g}_- t}}$. Let us show that $\hat{U}_-(t) = \exp[ir(\hat{A}^\dagger_{-,\mathrm{in}}(t)\hat{b}(0) + \mathrm{H.c.})]$ realizes the desired rotation $\hat{A}_{-,\mathrm{out}}(t) = \hat{U}_-^\dagger(t)\hat{A}_{-,\mathrm{in}}(t)\hat{U}_-(t)$ and $\hat{b}_-(t) = \hat{U}_-^\dagger(t)\hat{b}(0)\hat{U}_-(t)$. Writing $\hat{U}_-^\dagger(t) = \exp\hat{B}$, we have:

$$\hat{A}_{-,\mathrm{out}}(t) = e^{\hat{B}}\hat{A}_{-,\mathrm{in}}(t)e^{-\hat{B}}$$

$$= \sum_{k\in\mathbb{N}} \frac{1}{k!}\underbrace{[\hat{B},[\hat{B},\ldots,[\hat{B},\hat{A}_{-,\mathrm{in}}(t)]]]}_{k\text{ times}} \tag{A7}$$

$$= \sum_{k\in\mathbb{N}}\left[\frac{(-1)^k}{(2k)!}r^{2k}\hat{A}_{-,\mathrm{in}}(t) + i\frac{(-1)^k}{(2k+1)!}r^{2k+1}\hat{b}(0)\right] \tag{A8}$$

$$= \cos(r)\hat{A}_{-,\mathrm{in}}(t) + i\sin(r)\hat{b}(0) \tag{A9}$$

$$\hat{b}_-(t) = \cos(r)\hat{b}(0) + i\sin(r)\hat{A}_{-,\mathrm{in}}(t). \tag{A10}$$

Again, $\hat{U}_-(t) = \exp[ir(\hat{L}_+ + \hat{L}_-)]$ but this time the operators $\hat{L}_+ = \hat{L}_-^\dagger = \hat{A}^\dagger_{-,\mathrm{in}}(t)\hat{b}_-(0)$, $\hat{L}_0 = \hat{L}_0^\dagger = \frac{1}{2}[\hat{A}^\dagger_{-,\mathrm{in}}(t)\hat{A}_{-,\mathrm{in}}(t) - \hat{b}(0)\hat{b}^\dagger(0)]$ are three generators of the u(2) Lie algebra ($[\hat{L}_-,\hat{L}_+] = -2\hat{L}_0$, $[\hat{L}_0,\hat{L}_\pm] = \pm\hat{L}_\pm$). Then from Eq. (23a) of Ref. [28], one has:

$$\hat{U}_-(t) = e^{i\tan r\hat{A}^\dagger_{-,\mathrm{in}}\hat{b}(0)}(\cos r)^{-\hat{A}^\dagger_{-,\mathrm{in}}\hat{A}_{-,\mathrm{in}}+\hat{b}^\dagger(0)\hat{b}(0)}e^{i\tan r\hat{A}_{-,\mathrm{in}}\hat{b}^\dagger(0)}. \tag{A11}$$

APPENDIX B: APPROACHED ANALYTICAL CALCULATION

We develop an approached analytical description of the proposed protocol, providing an explicit expression of the mechanical density matrix after the first pulse in the simplified case where the detectors are photon-number resolving. We compute the probability for a coincidence event to happen, adding explanations to the results of Fig. 2. We then treat the red pulse and describe the contribution of dominant terms.

1. Blue pulse

We drop the + in this blue-detuned section. We start from the initial total optomechanical density matrix describing the two mechanical modes $\hat{b}_i$ as well as the two optical modes $\hat{A}_i$:

$$\rho_{\mathrm{tot,in}} = |0\rangle\langle 0|_{\hat{A}_1} \otimes |0\rangle\langle 0|_{\hat{A}_2} \otimes \rho^{th}_{b,1}(n_0) \otimes \rho^{th}_{b,2}(n_0) \tag{B1}$$

$$\rho^{th}_{b,i}(n_0) = (1 - p_i)\sum_{n_i} p_i^{n_i}|n_i\rangle\langle n_i|,\ p_i = n_{0i}/(1 + n_{0i}) \tag{B2}$$

and apply to each OM resonator the blue pulse evolution operator of duration T, allowing for various q_i and n_{0i}.

$$\rho_{\text{tot,out}} = \frac{(1-p_1)(1-p_2)}{(\cosh q_1 \cosh q_2)^2} \sum_{n_1,n_2,l_1,l_2,l_1,l_2} \bar{p_1}^{n_1} \bar{p_2}^{n_2} \Lambda(n_1,n_2,l_1,l_2,l_1,l_2)|l_1,l_2,n_1+l_1,n_2+l_2\rangle\langle l_1,l_2,n_1+l_1,n_2+l_2| \tag{B3}$$

with $\Lambda(n_1,n_2,l_1,l_2,l_1,l_2) = (i\tanh q_1)^{l_1}(i\tanh q_2)^{l_2}(-i\tanh q_1)^{l_1}(-i\tanh q_2)^{l_2}\sqrt{\frac{(n_1+l_1)!}{l_1!n_1!}}\sqrt{\frac{(n_2+l_2)!}{l_2!n_2!}}\sqrt{\frac{(n_1+l_1)!}{l_1!n_1!}}\sqrt{\frac{(n_2+l_2)!}{l_2!n_2!}}$ and $\bar{p}_i = p_i \cosh q_i^{-2}|l_1,l_2,n_1,n_2\rangle$ is the state with l_i photons at $_c$ and n_i phonons at Ω_m in the resonator OM_i.

After conditioning on the detection of one (and only one) photon with the projector $C = (|01\rangle\langle 01|_{A_1A_2} + |10\rangle\langle 10|_{A_1A_2}) \otimes \mathbb{I}_{b_1b_2}$ and tracing on the optical modes, we obtain the normalized bipartite mechanical state:

$$\rho^{\text{cond}}_{b_1b_2} = (1-\bar{p}_1)(1-\bar{p}_2)\sum \bar{p_1}^{n_1}\bar{p_2}^{n_2}\left(\frac{\tanh^2 q_1}{(1-\bar{p}_1)} + \frac{\tanh^2 q_2}{(1-\bar{p}_2)}\right)^{-1}$$
$$\times\ [\tanh^2 q_1(n_1+1)|n_1+1,n_2\rangle\langle n_1+1,n_2| + \tanh^2 q_2(n_2+1)|n_1,n_2+1\rangle\langle n_1,n_2+1|]. \tag{B4}$$

This last state corresponds to the situation investigated in Ref. [18]. We now treat the Bell state measurement. We restart from the unconditioned total density matrix after blue pulse and tensor product it with the to-be-teleported density matrix $\rho_c = \left(\begin{smallmatrix} |\alpha|^2 & \alpha\beta^* \\ \alpha^*\beta & |\beta|^2 \end{smallmatrix}\right)$ describing a photonic qubit in the H/V basis.

In order to condition on coincidences, i.e., on the Bell state $|\Psi^-\rangle = \frac{1}{\sqrt{2}}(|HV\rangle - |VH\rangle) \equiv \frac{1}{\sqrt{2}}(|H01\rangle - |V10\rangle)$ we employ the following conditioning operator, which acts before the Bell measurement beam splitter:

$$\hat{K} = \tfrac{1}{2}[|H01\rangle\langle H01| + |V10\rangle\langle V10| - |H01\rangle\langle V10| - |V10\rangle\langle H01|] \otimes \mathbb{I}_{b_1b_2}. \tag{B5}$$

After tracing on the optical modes, we obtain the unnormalized mechanical density matrix conditioned to a successful coincidence event:

$$\rho^{\text{cond,coin}} = \frac{(1-p_1)(1-p_2)}{2(\cosh q_1 \cosh q_2)^2} \sum_{n_1,n_2} \bar{p_1}^{n_1}\bar{p_2}^{n_2}|\Psi(n_1,n_2)\rangle\langle\Psi(n_1,n_2)| \tag{B6}$$

with $|\Psi(n_1,n_2)\rangle = \beta\tanh q_1\sqrt{n_1+1}|n_1+1,n_2\rangle - \alpha\tanh q_2\sqrt{n_2+1}|n_1,n_2+1\rangle$. The matrix must then be normalized:

$$\text{Tr}[\rho^{\text{cond,coin}}] = \Xi\Gamma \quad \text{with} \quad \Xi = \frac{(1-p_1)(1-p_2)}{2(\cosh q_1\cosh q_2)^2} \quad \text{and} \quad \Gamma = \frac{|\beta|^2\tanh^2 q_1}{(1-\bar{p}_1)^2(1-\bar{p}_2)} + \frac{|\alpha|^2\tanh^2 q_2}{(1-\bar{p}_2)^2(1-\bar{p}_1)}. \tag{B7}$$

Setting $q_1 = q_2$ and $p_1 = p_2$, we observe that the product $\Xi\Gamma$ is an increasing function of p, hence of n_0, which explains the results of Fig. 2. Finally, the normalized mechanical density matrix is:

$$\rho^{\text{cond,coin},*} = \Gamma^{-1}\sum_{n_1,n_2} \bar{p_1}^{n_1}\bar{p_2}^{n_2}|\Psi(n_1,n_2)\rangle\langle\Psi(n_1,n_2)|. \tag{B8}$$

2. Red pulse

For the red pulse, we compute the effect of the evolution operator on a generic mechanical state with the optical modes in the vacuum state:

$$\hat{U}^{\text{tot}}_-|0,0,n_1,n_2\rangle = \sum_{l_1\ n_1,l_2\ n_2} F(l_1,l_2,n_1,n_2)|l_1,l_2,n_1-l_1,n_2-l_2\rangle \tag{B9}$$

$$F(l_1,l_2,n_1,n_2) = \cos r_1^{n_1}\cos r_2^{n_2}(i\tan r_1)^{l_1}(i\tan r_2)^{l_2}\sqrt{\frac{n_1!}{(n_1-l_1)!l_1!}}\sqrt{\frac{n_2!}{(n_2-l_2)!l_2!}}. \tag{B10}$$

Such that the generic term in a density matrix evolves as:

$$\hat{U}^{\text{tot}}_-|0,0,n_1,n_2\rangle\langle 0,0,n_1,n_2|\hat{U}^{\text{tot},\dagger}_- \tag{B11}$$

$$= \sum_{l_1\ n_1,l_2\ n_2}\ \sum_{n_2\ l_1\ n_1,l_2\ n_2} F(l_1,l_2,n_1,n_2)F(l_1,l_2,n_1,n_2)^*|l_1,l_2,n_1-l_1,n_2-l_2\rangle\langle l_1,l_2,n_1-l_1,n_2-l_2|. \tag{B12}$$

We apply this formula to the four terms of $|0,0\rangle\otimes|\Psi(n_1,n_2)\rangle\langle\Psi(n_1,n_2)|\otimes\langle 0,0|$ for each (n_1,n_2) in Eq. (B8) before conditioning on one output photon with the projector $C = (|01\rangle\langle 01|_{A_1A_2} + |10\rangle\langle 10|_{A_1A_2})\otimes\mathbb{I}_{b_1b_2}$. Tracing on the mechanical modes leads to the final optical density matrix, which is analyzed by tomography at the end of the protocol. As an example, the

action of $\hat{U}_-^{\rm tot}$ on the dominant term of Eq. (B8) ($n_1 = n_2 = 0$) finally results in the following optical density matrix:

$$\begin{aligned}
&\mathrm{Tr}_{\rm mech}[\hat{U}_-^{\rm tot}|0,0\rangle \otimes |\Psi(0,0)\rangle\langle\Psi(0,0)| \otimes \langle 0,0|\hat{U}_-^{\rm tot,\dagger}] \\
&\quad = \{|F(0,0,1,0)|^2|\beta|^2 \tanh^2 q_1 + |F(0,0,0,1)|^2|\alpha|^2 \tanh^2 q_2\}|00\rangle\langle 00| + |F(1,0,1,0)|^2|\beta|^2 \tanh^2 q_1 |10\rangle\langle 10| \\
&\qquad + |F(0,1,0,1)|^2|\alpha|^2 \tanh^2 q_2 |01\rangle\langle 01| - F(1,0,1,0)F^*(0,1,0,1)\beta\alpha^* \tanh q_1 \tanh q_2 |10\rangle\langle 01| \\
&\qquad - F^*(1,0,1,0)F(0,1,0,1)\beta^*\alpha \tanh q_1 \tanh q_2 |01\rangle\langle 10|.
\end{aligned} \tag{B13}$$

We recall that in this notation $|10\rangle \equiv |H\rangle$ and $|01\rangle \equiv |V\rangle$. Projecting on the nonvacuum state removes the first line and assuming ($r_1 = r_2$, $q_1 = q_2$) leaves us with a density matrix proportional to: $\left(\begin{smallmatrix} |\beta^2| & -\beta\alpha^* \\ -\beta^*\alpha & |\alpha|^2 \end{smallmatrix}\right) = \sigma_z\sigma_x\rho_c\sigma_x\sigma_z$ in the H/V basis. The calculation for the next term ($n_1 = 1, n_2 = 0$) leads to the following result:

$$\begin{aligned}
&\mathrm{Tr}_{\rm mech}[\hat{U}_-^{\rm tot}|0,0,\Psi(1,0)\rangle\langle 0,0,\Psi(1,0)|\hat{U}_-^{\rm tot,\dagger}] \\
&\quad = \{2|F(0,0,2,0)|^2|\beta|^2 \tanh^2 q_1 + |F(0,0,1,1)|^2|\alpha|^2 \tanh^2 q_2\}|00\rangle\langle 00| \\
&\qquad + \Big(2|F(1,0,2,0)|^2|\beta|^2 \tanh^2 q_1 + \overbrace{|F(1,0,1,1)|^2|\alpha|^2 \tanh^2 q_2}^{\text{parasitic term}}\Big)|10\rangle\langle 10| + |F(0,1,1,1)|^2|\alpha|^2 \tanh^2 q_2 |01\rangle\langle 01| \\
&\qquad - \sqrt{2}\beta\alpha^* \tanh q_1 \tanh q_2 F(1,0,2,0)F^*(0,1,1,1)|10\rangle\langle 01| - \sqrt{2}\beta^*\alpha \tanh q_1 \tanh q_2 F(0,1,1,1)F^*(1,0,2,0)|01\rangle\langle 10| \\
&\qquad + 2|F(2,0,2,0)|^2|\beta|^2 \tanh^2 q_1 |20\rangle\langle 20| + |F(1,1,1,1)|^2|\alpha|^2 \tanh^2 q_2 |11\rangle\langle 11| \\
&\qquad - \sqrt{2}\beta\alpha^* \tanh q_1 \tanh q_2 F(2,0,2,0)F^*(1,1,1,1)|20\rangle\langle 11| - \sqrt{2}\beta^*\alpha \tanh q_1 \tanh q_2 F(1,1,1,1)F^*(2,0,2,0)|11\rangle\langle 20|,
\end{aligned} \tag{B14}$$

where multiphoton states are present that degrade the computed fidelity. A parasitic term proportional to $|\alpha|^2$ induces a finite matrix element $|10\rangle\langle 10|$ even if $\beta = 0$. This makes the fidelity state dependent as discussed in Appendix C.

3. Realistic projectors

The above calculation is simplified since we considered ideal photon-number resolving detectors, allowing us to express $\hat{K}$ with only two-photon states. The numerical simulations presented in the main text apply instead a 50:50 beam-splitter interaction before conditioning on coincidence events in the four output modes of the Bell state measurement beam splitter (two polarization modes $H/V \times$ two spatial modes L/R) with the following projector, which acts after the beam splitter:

$$\hat{K} = \left(\mathbb{I}_{L_H L_V R_H R_V} - (1-\eta_{\rm detect})^2|0000\rangle\langle 0000| - (1-\eta_{\rm detect}) \sum_{(i,j)\neq(0,0)} |00ij\rangle\langle 00ij| + |ij00\rangle\langle ij00|\right) \otimes \mathbb{I}_{b_1 b_2}. \tag{B15}$$

where we took into account the detector's dark count rate $\Gamma_{\rm dark}$. Let $\Gamma_{\rm rep}$ be the repetition rate of the protocol, a click on a detector has a probability $\eta_{\rm detect} = \Gamma_{\rm dark}/(\Gamma_{\rm dark} + \Gamma_{\rm rep})$ to be a false positive. Similarly the right projector to use during the red pulse is $\hat{C} = [\mathbb{I}_{A_1 A_2} - (1-\eta_{\rm detect})|00\rangle\langle 00|] \otimes \mathbb{I}_{b_1 b_2}$ in order to allow for multiple-photon states to be treated by the tomography unit with noisy detectors.

APPENDIX C: TECHNICAL CHALLENGES

1. Noise equivalent phonon number

As shown in Fig. 2 high fidelities are attained for low interaction strengths $\tilde{g}_\pm T_\pm$. For fixed device parameters g_0 and κ, there is hence an upper bound to the product $n_c T_\pm$. In addition a minimal n_c is required, which prevents from arbitrarily increasing $T_\pm$. This is shown by an analysis of the noise-equivalent phonon number n_{NEP}, a figure already introduced in past work [26]:

$$n_{NEP} = \frac{\Gamma_{\rm dark} + \Gamma_{\rm pump}}{\Gamma_{SB}} = \frac{\kappa^2 \Gamma_{\rm dark}}{4\kappa_e \eta g_0^2 n_c} + A\left(\frac{\kappa\Omega_m}{2\kappa_e g_0}\right)^2 \tag{C1}$$

with $\Gamma_{\rm dark}$ the dark-count rate of the photodetectors, $\Gamma_{\rm pump}$ the arrival rate of pump photons that are not properly filtered and leak to the detection, Γ_{SB} the sideband photon rate, A the attenuation factor from the filter and η the total measurement efficiency, including optical losses from the resonator to the detectors and detector efficiency. In Fig. 3, we plot n_{NEP} as a function of n_c and η for the parameters of Sec. IV C, but for the optical coupling, which we assume to be critical $\kappa = 2\kappa_e$. We consider $A = -100$ dB and $\Gamma_{\rm dark} = 100$ Hz.

With such strong filtering but limited detection efficiency, a value of $n_c \geqslant 100$ is required to maintain n_{NEP} below 0.1. Combining this constraint with the bound on $n_c T$ explains why $T_\pm$ cannot be increased arbitrarily, hence our choice of $T_\pm = 10$ ns.

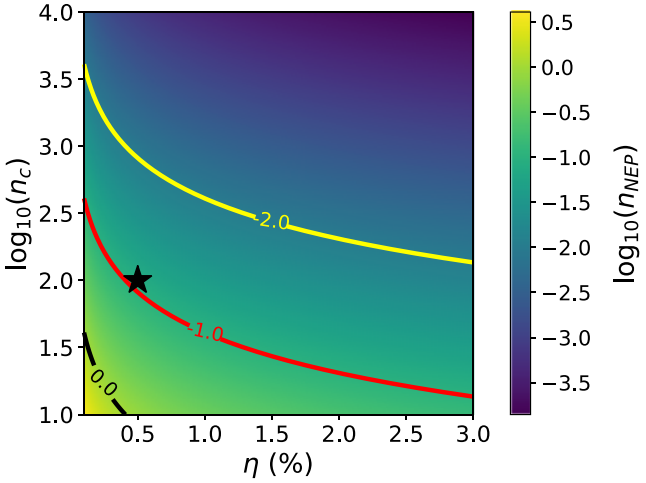

FIG. 3. Noise-equivalent phonon number as a function of intracavity photon number n_c and total optical detection efficiency η. The black star corresponds to the parameters considered in the text and ensures that n_{NEP} 0.1.

2. Waiting time and probability of success in experiments

We wish to estimate the minimal waiting time between two successful completions of the protocol, i.e., a coincidence event during step (i) followed by a detection event on one of the detectors during step (ii). We impose a maximal duration T_{off} γ_m^{-1} between the blue and the red pulse, in order to protect the coherence of the generated mechanical state. Numerical simulations show indeed that the fidelity of the mechanical state generated by the blue pulse decays approximately like $e^{-\gamma_m t/2}$ over the first few γ_m^{-1}. But in order to ensure that the devices are at equilibrium with the thermal bath, we also wait at least T_{relax} (typically more than a few γ_m^{-1}) between two realizations of the protocol. The time taken to realize the protocol and reinitialize the setup is then $T_{\text{per}} = T_+ + T_{\text{off}} + T_- + T_{\text{relax}}$. The probability of success of the whole protocol (teleportation and read out) is $p_{\text{success}} = (\eta_{sps} \cdot \eta_+ p_+ \cdot \eta_- p_-)$, with $\eta_\pm$ the linear efficiencies of the two subsequent optical measurements associated to steps (i) and (ii) and η_{sps} the efficiency of the single-photon source whose photon states are to be teleported. Since T_{per} is dominated by T_{relax}, one can think of reducing the mechanical quality of the devices in order to decrease $T_{\text{per}}/p_{\text{success}}$, but this will affect their memory capabilities. Since small values of $p_\pm$ are required to ensure large fidelities, it is crucial to develop efficient filtering and optical detection paths.

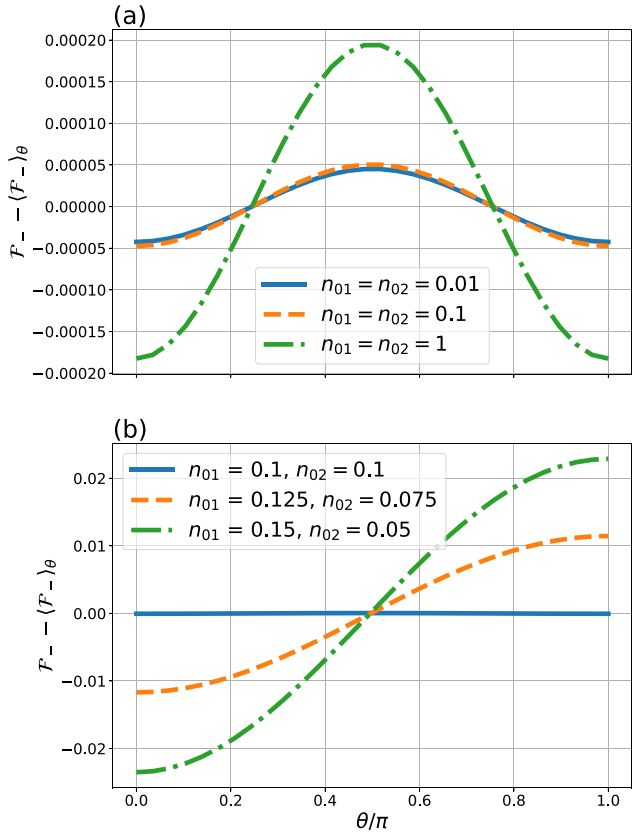

FIG. 4. Fidelity after the red pulse as a function of the initial state to teleport $|\Phi(\theta,\varphi)\rangle = \cos(\theta/2)|H\rangle + e^{i\varphi}\sin(\theta/2)|V\rangle$, $\forall\varphi$. For all plots, $\tilde{g}_\pm T_\pm/2\pi = 4.9\times10^{-3}$.

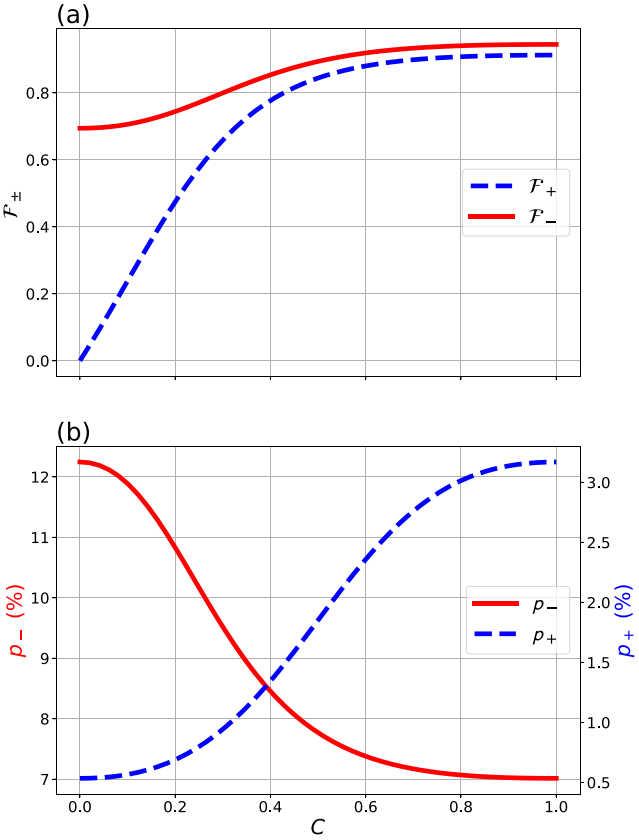

FIG. 5. (a) Fidelities and (b) probabilities of success of the two steps of the protocol with respect to C. The parameters are those considered in the text.

3. Nonidentical resonators

In practice, the two nanofabricated optomechanical devices will present differences in their exact dimensions, typically at the part per thousand level or less [29], producing a detuning

in their optical and mechanical frequencies. Differences in their optical and/or mechanical dissipation can also be sizable. Part of this problem can be compensated by driving in an asymmetric way [18]. One can shift the drive frequency to match the mechanical sideband and balance the drive power in the two arms in order to compensate for different g_0^2/κ ratio. However, a difference in Ω_m implies that the two mechanical degrees of freedom precess at different speeds during the off time between pulses, producing an evolutive dephasing. Moreover the need for indistinguishable photons after scattering in both devices puts a central constraint on their cavity frequency: $|\ _{c1} - \ _{c2}|$ should be as low as possible. These aspects can be treated by the use of postprocess techniques to reduce the resonator-to-resonator disorder, such as the photoelectrochemical tuning technique demonstrated in nano-optomechanical devices [29].

4. Dependence on α and β

An interesting feature is that all states on the Bloch sphere are not equally handled by the protocol. Indeed, even for equal initial phonon occupancy of the two disks, equatorial states are retrieved with a better fidelity after the red pulse [see Fig. 4(a)]. If the state to teleport sits on the pole ($\alpha = 1$, $\beta = 0$ for instance), the two resonators must be placed in the phononic state $|01\rangle$. There should be zero horizontal component in the polarization of the output photon after the red pulse, which is not possible since the true phononic occupancy of OM_1 is always larger than 0. In contrast, teleporting an equatorial state $|\alpha| = |\beta|$ is easier because the photon we expect has equal horizontal and vertical polarization components, which is naturally achieved in our balanced Mach-Zehnder configuration. This subtle effect is larger as the mean initial phonon occupancy of the disks grows, and the states that are easier to read out shift away from the equator as we introduce an imbalance in the initial occupancy of the two disks [see Fig. 4(b)].

5. Importance for $\ \rangle$ to be in a single-photon state

One could imagine using a strongly attenuated coherent source instead of a single-photon source for the Bell measurement, but this would strongly impact the implementation of the protocol. In fact, such attenuated coherent state (with mean photon occupancy $\ll 1$) overlaps mostly with the vacuum state, hence produces most of the time no useful coincidence. Additionally a coincidence event in our measurement does not mean necessarily that one photon from the source and one photon from the Mach-Zehnder interferometer were successfully projected in the antisymmetric Bell state $|\Psi^-\rangle$ before the beam splitter. Coincidence events also take place when a wave packet containing several photons exits the interferometer and impinges on the Bell measurement beam splitter, postselecting undesirable multiexcitation events. This can be appreciated writing $|\Phi(C)\rangle = \sqrt{1-C}|0\rangle + \sqrt{C}(\alpha|H\rangle + \beta|V\rangle)$ and looking at the fidelities and probabilities of success with respect to C in Fig. 5. As expected, $\ _{\pm}$ is degraded at low C, but p_- increases because events where more than one phonon was created were selected during (i). This stresses the advantage of using an ideal single-photon source as input of the protocol.

[1] C. H. Bennett, G. Brassard, C. Crépeau, R. Jozsa, A. Peres, and W. K. Wootters, Phys. Rev. Lett. **70**, 1895 (1993).

[2] D. Bouwmeester, J. W. Pan, K. Mattle, M. Eibl, H. Weinfurter, and A. Zeilinger, Nature (London) **390**, 575 (1997).

[3] A. Furusawa, J. L. Sørensen, S. L. Braunstein, C. A. Fuchs, H. J. Kimble, and E. S. Polzik, Science **282**, 706 (1998).

[4] M. A. Nielsen, E. Knill, and R. Laflamme, Nature (London) **396**, 52 (1998).

[5] M. Riebe, H. Häffner, C. F. Roos, W. Hänsel, J. Benhelm, G. P. T. Lancaster, T. W. Körber, C. Becher, F. Schmidt-Kaler, D. F. V. James, and R. Blatt, Nature (London) **429**, 734 (2004).

[6] M. D. Barrett, J. Chiaverini, T. Schaetz, J. Britton, W. M. Itano, J. D. Jost, E. Knill, C. Langer, D. Leibfried, R. Ozeri, and D. J. Wineland, Nature (London) **429**, 737 (2004).

[7] S. M. Olmschenk, D. N. Matsukevich, P. Maunz, D. Hayes, L. M. Duan, and C. Monroe, Science **323**, 486 (2009).

[8] W. B. Gao, P. Fallahi, E. Togan, A. Delteil, Y. S. Chin, J. Miguel-Sanchez, and A. Imamoğlu, Nat. Commun. **4**, 2744 (2013).

[9] W. Pfaff, B. J. Hensen, H. Bernien, S. B. van Dam, M. S. Blok, T. H. Taminiau, M. J. Tiggelman, R. N. Schouten, M. Markham, D. J. Twitchen, and R. Hanson, Science **345**, 532 (2014).

[10] K. S. Chou, J. Z. Blumoff, C. S. Wang, P. C. Reinhold, C. J. Axline, Y. Y. Gao, L. Frunzio, M. H. Devoret, L. Jiang, and R. J. Schoelkopf, Nature (London) **561**, 368 (2018).

[11] S. Mancini, D. Vitali, and P. Tombesi, Phys. Rev. Lett. **90**, 137901 (2003).

[12] S. Pirandola, S. Mancini, D. Vitali, and P. Tombesi, Phys. Rev. A **68**, 062317 (2003).

[13] S. G. Hofer, W. Wieczorek, M. Aspelmeyer, and K. Hammerer, Phys. Rev. A **84**, 052327 (2011).

[14] S. Felicetti, S. Fedortchenko, R. Rossi, S. Ducci, I. Favero, T. Coudreau, and P. Milman, Phys. Rev. A **95**, 022322 (2017).

[15] M. Eichenfield, J. Chan, R. M. Camacho, K. J. Vahala, and O. Painter, Nature (London) **462**, 78 (2004).

[16] L. Ding, C. Baker, P. Senellart, A. Lemaître, S. Ducci, G. Leo, and I. Favero, Phys. Rev. Lett. **105**, 263903 (2010).

[17] L. Ding, C. Baker, P. Senellart, A. Lemaître, S. Ducci, G. Leo, and I. Favero, Appl. Phys. Lett. **98**, 113108 (2011).

[18] R. Riedinger, A. Wallucks, I. Marinković, C. Löschnauer, M. Aspelmeyer, S. Hong, and S. Gröblacher, Nature (London) **556**, 473 (2018).

[19] I. Marinković, A. Wallucks, R. Riedinger, S. Hong, M. Aspelmeyer, and S. Gröblacher, Phys. Rev. Lett. **121**, 220404 (2018).

[20] A. Wallucks, I. Marinković, B. Hensen, R. Stockhill, and S. Gröblacher, Nat. Phys. (2020).

[21] M. Hamoumi, P. E. Allain, W. Hease, E. Gil-Santos, L. Morgenroth, B. Gérard, A. Lemaître, G. Leo, and I. Favero, Phys. Rev. Lett. **120**, 223601 (2018).

[22] G. S. MacCabe, J. L. Hengjiang Ren, J. D. Cohen, H. Zhou, M. M. Alp Sipahigil, and O. Painter, arXiv:1901.04129.

[23] M. J. Woolley and A. A. Clerk, Phys. Rev. A **87**, 063846 (2013).
[24] C. Galland, N. Sangouard, N. Piro, N. Gisin, and T. J. Kippenberg, Phys. Rev. Lett. **112**, 143602 (2014).
[25] V. C. Vivoli, T. Barnea, C. Galland, and N. Sangouard, Phys. Rev. Lett. **116**, 070405 (2016).
[26] S. M. Meenehan, J. D. Cohen, G. S. MacCabe, F. Marsili, M. D. Shaw, and O. Painter, Phys. Rev. X **5**, 041002 (2015).
[27] J. Li, A. Wallucks, R. Benevides, N. Fiaschi, B. Hensen, T. P. M. Alegre, and S. Gröblacher, arXiv:2005.08860.
[28] D. R. Truax, Phys. Rev. D **31**, 1988 (1985).
[29] E. Gil-Santos, C. Baker, A. Lemaître, S. Ducci, C. Gomez, G. Leo, and I. Favero, Nat. Commun. **8**, 14267 (2017).